Shap. Mem. Superelasticity (2021) 7:235–249
https://doi.org/10.1007/s40830-021-00335-0

TECHNICAL ARTICLE

Unraveling Frequency Effects in Shape Memory Alloys: NiTi and FeMnAlNi

R. Sidharth[1] · A. S. K. Mohammed[1] · W. Abuzaid[2] · H. Sehitoglu[1]

Received: 11 February 2021 / Revised: 16 April 2021 / Accepted: 26 May 2021 / Published online: 18 June 2021

Abstract With the presence of internal interfaces such as the austenite–martensite interface and the internal twin boundaries in the martensite, shape memory alloys (SMAs) can be employed in passive/active damping applications. Due to the latent heat of transformation, a temperature rise/drop during a load/unload cycle is expected to dynamically couple with the mechanical response of the SMA and influence the stress levels of forward/reverse transformation and thus the hysteretic area (i.e. the dissipated energy). Additionally, the temperature change per cycle is a function of loading frequency due to momentary heat transfer effects. To this end, for the first time, we demonstrate a rate insensitive shape memory alloy system, $Fe_{43.5}Mn_{34}Al_{15}Ni_{7.5}$ which also exhibits near-zero temperature dependent stress–strain response. Contrastingly, we show that $Ni_{50.8}Ti$, which is widely used commercially, is highly rate sensitive. With straightforward in situ experiments, complemented with thermomechanical modelling, we pinpoint the key material parameter which dictates frequency sensitivity. The corresponding results are then discussed in the light of different mechanisms contributing to the damping capacity of SMAs.

Keywords Superelasticity · Damping capacity · Hysteresis · Latent heat · Entropy of transformation · Clausius-Clapeyron · Internal friction

Introduction

Since their advent in 1938 [1], shape memory alloys (SMAs) have become one of the most successful functional materials of today. To name a few applications, they are commercially used as smart structures, seismic dampers, biomedical implants and solid-state actuators across biomedical, automotive, civil and aerospace domains [2–11]. Within a suitable temperature window of operation, an external load applied to an SMA triggers a martensitic phase transformation allowing the material to accommodate large deformation. Upon unloading, the transformation reverses to allow near-perfect recovery of the applied strain, key to the functional success of this class of materials. This phenomenon, termed as "superelasticity", is accompanied by a dissipation of energy (hysteresis) during the load-unload cycle. This loss is interpreted as energy dissipated due to "Internal Friction" (IF) in the material, caused by several material mechanisms [12–15] which ultimately dictate the damping capacity of SMAs [16]. It is worth noting that the damping capacity of SMAs is typically an order of magnitude higher than conventional steels [15, 17]. This study analyzes the dependence of the hysteresis on the frequency of applied load on two starkly contrasting SMA systems, establishing the key

This article is part of a special topical focus in *Shape Memory and Superelasticity* on the Mechanics and Physics of Active Materials and Systems. This issue was organized by Dr. Theocharis Baxevanis, University of Houston; Dr. Dimitris Lagoudas, Texas A&M University; and Dr. Ibrahim Karaman, Texas A&M University.

✉ R. Sidharth
ravi8@illinois.edu

✉ H. Sehitoglu
huseyin@illinois.edu

[1] Department of Mechanical Science and Engineering, University of Illinois at Urbana-Champaign, 1206 W. Green St, Urbana, IL 61801, USA

[2] Department of Mechanical Engineering, American University of Sharjah, PO Box 26666, Sharjah, United Arab Emirates

transformation trait that can diminish or exacerbate the frequency-sensitivity of hysteresis.

The sensitivity of hysteresis to load–frequency has been a subject of interest in SMAs since the last two decades. This sensitivity has been studied primarily by two approaches. One approach is via dynamic testing, using experiments such as Dynamic Mechanical Analysis (DMA) to characterize the IF based on the phase-lag between the oscillatory load-input and output strain-response [13–15, 18–22]. In the second approach, the effect of load–frequency was studied in the form of strain-rate dependence of superelastic mechanical response, characterized by uniaxial tension/compression tests [23–37]. The total IF in this mode is quantified as the ratio between the dissipated energy (area under the stress strain loop) and the total stored elastic strain energy [38]. In both modalities, strong frequency-dependence of the IF was pointed out, observing significant variation of the hysteresis with change of frequency. This variation of IF per load-cycle has drastic implications on the fatigue life of the SMA [39–41]. It is hence imperative to find candidate SMAs insensitive to load–frequency.

In order to reach this goal, the underlying material mechanisms contributing to the IF (hysteresis) need to be better understood. While such an understanding has been established in the aforementioned dynamic approach [14, 15, 18], an equivalent description in superelastic response is lacking. We introduce the partitioning of superelastic hysteresis into three contributions analogous to propositions in [14, 15, 18]: (i) transitory part, (ii) phase transformation part and (iii) intrinsic part. Figure 1 schematically shows the effect of each contribution on the stress hysteresis in a superelastic deformation.

Contribution (i): The transitory term depends on the transformation kinetics and accounts for the friction of the A/M interface. It is a function of the rate of evolution of martensite which successively depends on the stress rate (Fig. 1a). Consequently, the latent heat trapped within the sample during forward transformation and the associated temperature change should depend on loading frequency. Prior studies have presumed that the transitory contribution is insignificant under ambient isothermal conditions [14, 15, 42], such as in a superelastic deformation. However, a superelastic deformation is always accompanied by self-heating/cooling of the sample. Even when the loading/unloading rate is symmetric, the temperature evolution rate can be asymmetric and is expected to affect the stress levels of the forward/reverse transformation and hence the damping capacity. Due to the heat transfer into the ambient environment, the temperature change during superelastic deformation is negligible (isothermal conditions) at very low loading frequencies (< 0.0001 Hz) [29, 32] and reaches a steady state (symmetric temperature change) when adiabatic conditions are approached at higher frequencies (> 20 Hz), hence the transient nature of the internal friction in a superelastic deformation.

Contribution (ii): The next dominant contribution to the internal friction is by the phase transformation part [14, 18, 43]. Melton and Mercier showed that this term arises due to dislocation dissipation processes occurring during the A/M transformation [44]. Their model accounts for the change in elastic modulus during phase transformation which affects the elastic strain energy of dislocations and thus the dislocation damping behavior. In a broader sense, this term is a consequence of the mechanism of phase transformation which influences the various plastic dissipation processes (Fig. 1b). The respective crystal structures of austenite and martensite, the lattice correspondences, loading orientation, twin thickness of internally twinned martensite and the resultant coherency strains at the A/M interface [45–52] are few of the main factors influencing the phase transformation mechanism. Under functional cycling the repeated dislocation emission [51, 53, 54] and the resulting internal stress generated by dislocation accumulation will influence the specific damping capacity. As the magnitudes of inelastic strains stabilize, the specific damping capacity determined by contribution (ii) should stabilize as well.

Contribution (iii): The final contribution to the internal friction is attributed to the intrinsic damping capacity of either of the austenite and martensite phases. In the case of internally twinned martensite, it is highly dependent on the density of twin interface, and twin migration energy [15]. The specific damping capacity of the twin interface is essentially influenced by the frictional resistance to the twin partials, partial density, amplitude of motion and burgers vector [55]. Assuming that the partial motion is completely reversible, this term does not account for plastic dissipation within martensite (Fig. 1c) [14, 15, 55]. In austenite, it depends on vacancy concentration and matrix dislocation density, however the specific damping capacity is negligible compared to that of martensite [14, 15, 43].

Of the three contributions mentioned above, the transitory component exhibits highest sensitivity to the applied strain-rate or equivalently the load frequency. This sensitivity pertains to the latent heat of transformation and consequently least-sensitivity can be obtained from a SMA exhibiting low latent heat or more precisely, a low enthalpy-change (ΔH) during phase-transformation. The ideal candidate as of today is the newly developed Fe-based SMA FeMnAlNi [56–59]. It exhibits possibly the lowest Clausius-Clapeyron slope ($d\sigma/dT$), which takes into account the change in transformation stress with respect to temperature, of all SMAs [58, 59] owing to its low enthalpy-change (ΔH) and entropy-change (ΔS) during transformation. The entropy-change ΔS is of the order of -0.4 J/mol/K starkly contrasting that of NiTi which

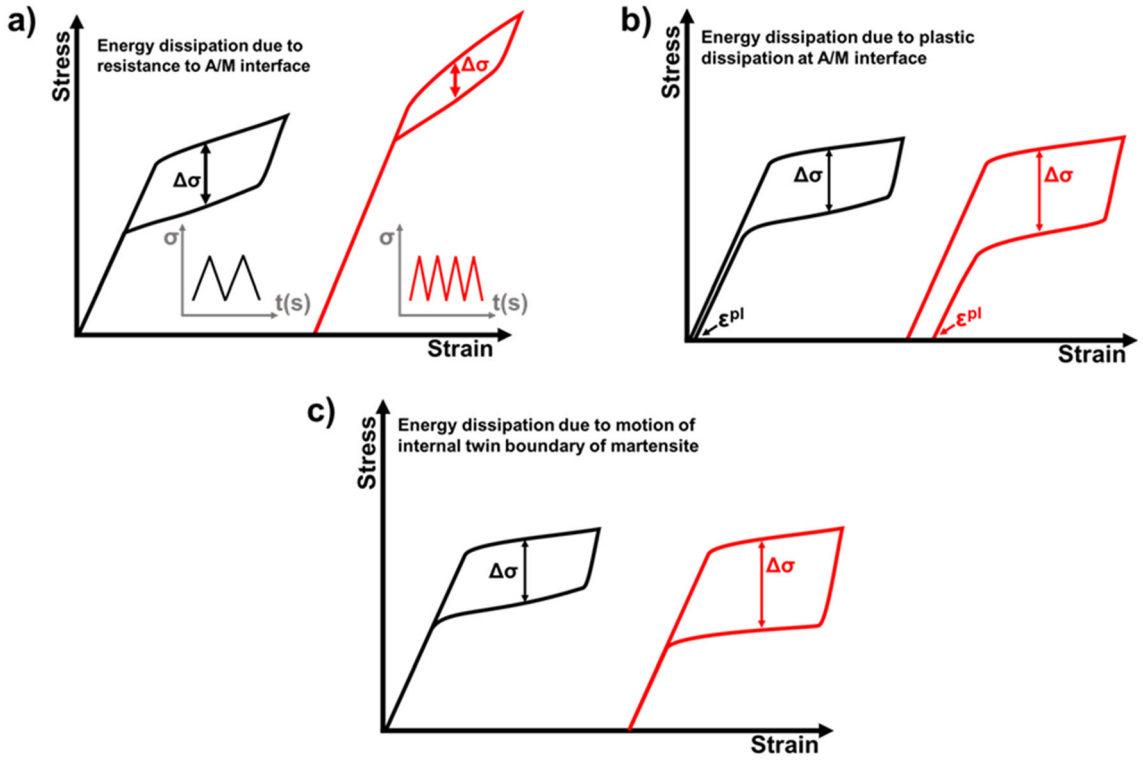

Fig. 1 A schematic to elucidate the change in stress–strain response and the hysteresis loop area as influenced by different contributions to the total internal friction such as the **a** transitory part, **b** phase transformation part, and **c** intrinsic part. The sub-figure in **a** is a schematic depicting low and high loading rates (Color figure online)

exhibits an entropy-change of the order −4 J/mol/K [59]. Consequently, FeMnAlNi offers the widest temperature-window for superelasticity or "functionality" (> 400 °C) [57], again contrasting with NiTi exhibiting a temperature window of functionality < 100 °C. Additionally, FeMnAlNi is inexpensive, has good weldability [60] and exhibits local transformation strains exceeding 10% [57, 61]. Thus it offers a promising alternative to NiTi which despite limitations of high cost, poor workability and narrow window of functionality, is one of the most commercially successful SMAs [62, 63].

In this study, we examine the frequency dependence of hysteresis in $Fe_{43.5}Mn_{34}Al_{15}Ni_{7.5}$ for the first time and contrast it with that of $Ni_{50.8}Ti$, highlighting one of the key intrinsic material parameters responsible for rate-sensitivity in superelasticity. The frequency range is chosen as 0.01–10 Hz, covering low-frequency quasi-static test regimes to higher frequencies expected in practical applications such as in space structures and seismic structures [64, 65]. Furthermore, all aforementioned studies focused on studying polycrystalline samples. The stress hysteresis is expected to be affected by grain boundary interactions [66] and to study the intrinsic response of the SMA, single crystals are employed in this study. High-speed non-contact IR thermography will be used to monitor the spatial temperature change on the sample surface and will be correlated with the change in stress hysteresis with respect to the loading frequency. High-speed optical camera will be utilized to obtain in situ optical images for Digital Image Correlation (DIC) to reproduce the stress strain curves. Both non-contact methods serve as an essential tool to accurately map the spatial evolution of temperature and strain fields and are used as an input for a simple analytical thermomechanical model. Several thermomechanical models have simulated frequency-dependent behavior of SMAs [67–71]. We employ the analytical thermomechanical model motivated from the studies in [72–74]. The focus of the model is to contrast the behavior of two SMA systems considered to narrow down the key material parameter dictating frequency-sensitivity. In that regard, the model is not meant to be predictive but rather instructive of underlying behavior causing the observed frequency dependence.

Materials and Methods

In this study $Ni_{50.8}Ti$ and $Fe_{43.5}Mn_{34}Al_{15}Ni_{7.5}$ (at %) single crystals were used. The single crystals were grown using Bridgeman technique in an inert environment. The inverse pole figure (IPF) of different NiTi and FeMnAlNi single crystals are shown in Fig. 2. $Ni_{50.8}Ti$ single crystal ingots were solutionized at 920 °C for 24 h in inert atmosphere

and water quenched. Then miniature compression samples of 4 × 4 × 8mm dimension were EDM cut out of the ingot and aged at 550 °C for 1.5 h and water quenched to produce coherent, homogenous Ni_4Ti_3 precipitates in the matrix [74]. FeMnAlNi single crystal ingots were also EDM cut into 4 × 4 × 8mm samples and encapsulated in quartz tubes with residual argon pressure < 50mTorr. The samples were then solutionized at 1300 °C for 1 h and quenched in 80 °C water [56]. Subsequently, the samples were aged at 225 °C for 4 h to introduce coherent B2 NiAl precipitates which partially order the BCC austenite matrix and promote thermoelastic martensitic transformation [75].

Prior to loading, all samples (about 20–25 for each material) were mechanically polished with abrasive papers up to P4000 and finished with 1 µm suspended alumina to achieve mirror surface finish. 600 grit SiC powder was air blasted on the polished surface to obtain the DIC pattern for full-field strain measurements. On the back side, the surface was coarse ground with P400 abrasive paper and airbrushed with black paint for IR thermography. The uniaxial compression experiments were performed on an Instron servo hydraulic load frame under displacement control at different loading rates ranging from 0.01 Hz to 10 Hz. At this point it should be noted that different samples were used for all the loading frequencies and the data reported is for a single-cycle test devoid of any fatigue-related effects. The images for DIC were taken by an FLIR-ORX-10G-51S5M high speed camera operating in the range of 1fps for low frequency test to 500fps for the high frequency test. The corresponding spatial resolution of the images was of the order of 3 µm/pixel. The DIC strain field within this area of interest was determined using a commercial software VIC-2D. For thermography, FLIR A6753 IR camera was used at frame rates of 25fps to 394fps for low frequency and high frequency tests, respectively. The IR camera was calibrated for a temperature range of 10–90 °C. All the experiments were performed at room temperature. Dual camera setup (Fig. 2a) was employed to obtain images for DIC and IR thermography simultaneously.

Experimental Results

Frequency Effects on the Stress–strain Response

Representative stress–strain response of NiTi is shown in Fig. 3. The local strains and the global strains extracted from DIC was plotted against the nominal applied stress. It elucidates that the sample undergoes a rather inhomogeneous deformation with different volumes of the sample exhibiting different levels of strains. Consequently, the temperature evolution from the stress induced phase transformation is also concentrated locally. As shown in Fig. 3, the local strains reach up to 5% and the sample heats up locally to 3.1 °C during loading and cools down by 5.4 °C during unloading. The magnitude of self-heating/cooling is indeed affected by the rate of loading due to heat transfer effects. Figure 4a shows the frequency effect on stress hysteresis for NiTi and FeMnAlNi. The hysteresis was calculated as the maximum difference between the stresses during forward transformation and reverse transformation ($\Delta\sigma$). The hysteresis was normalized with 0.1% transformation stress to account for sample-to-sample variabilities in the microstructure. The maximum applied strains were comparable (i.e., 1.8 to 2%) in all samples to minimize amplitude effects on hysteresis. It is clear that the stress hysteresis, and thus the damping capacity (Fig. 9), is

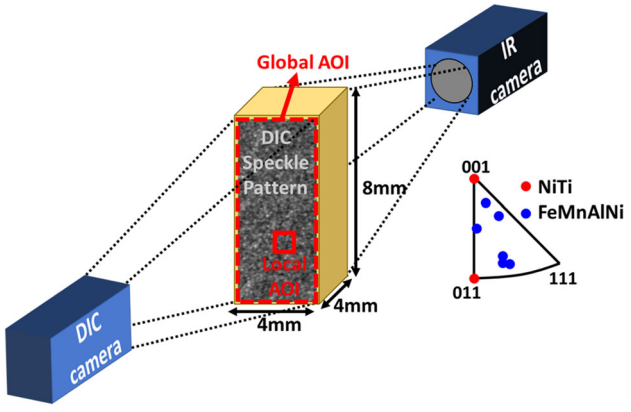

Fig. 2 Dual camera setup to facilitate simultaneous real-time DIC and IR measurements and the Inverse pole figure (IPF) representing all the loading orientations investigated. Note that the local AOI is not drawn to scale and the location of local AOI differs from sample to sample (Color figure online)

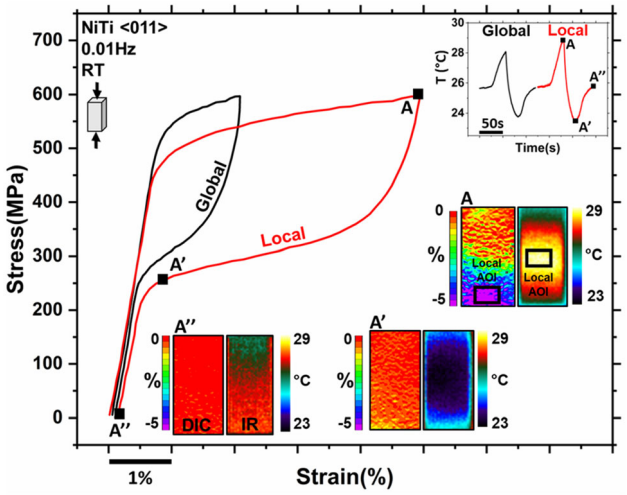

Fig. 3 Stress–Strain curve of NiTi < 011 > at 0.01 Hz loading frequency elucidating the local and global response

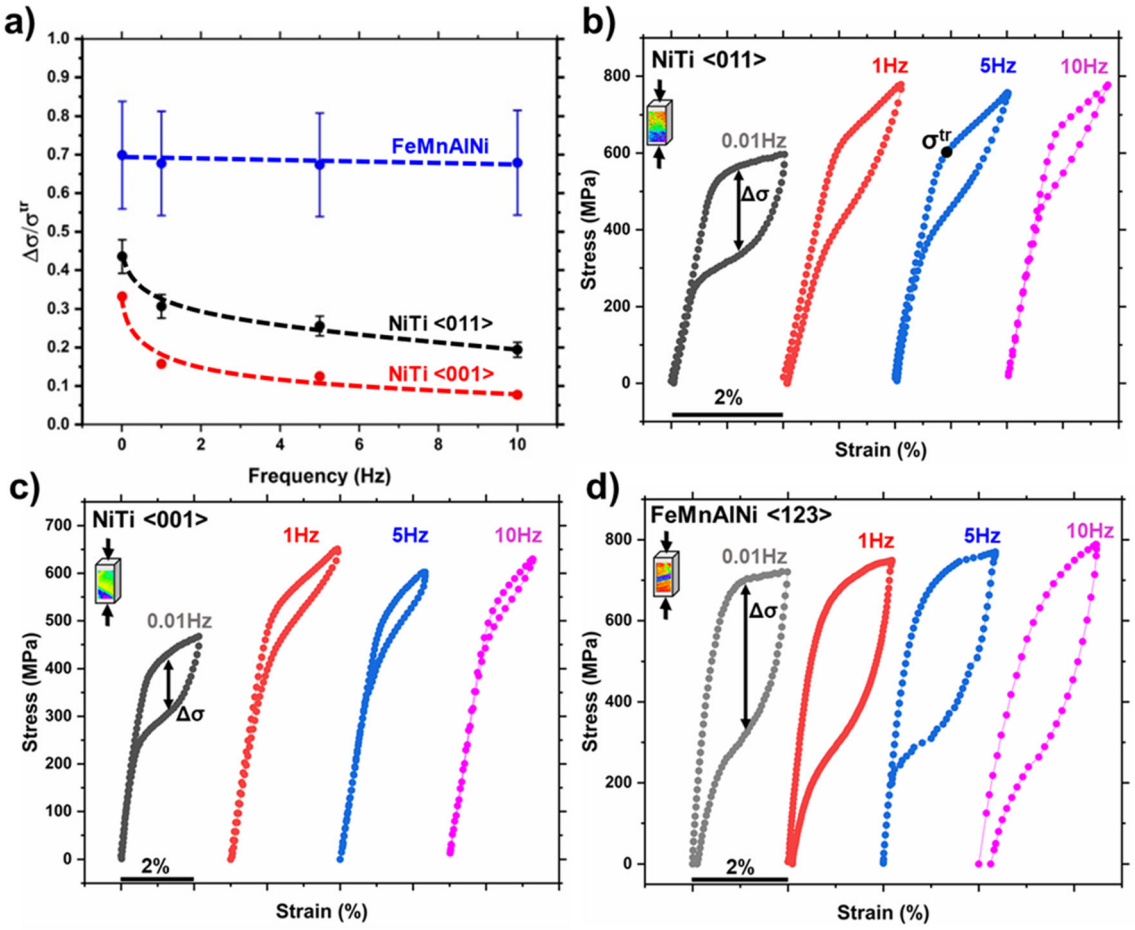

Fig. 4 **a** Stress hysteresis vs loading frequency. Global Stress–Strain curve for **b** NiTi $< 011 >$, **c** NiTi $< 001 >$, **d** all the orientations of FeMnAlNi. 0.1% transformation stress was used for normalizing

decreasing with increasing loading frequency for NiTi. On the other hand, FeMnAlNi differs and exhibits a fairly constant hysteresis but with higher variability which can be linked to the quenched microstructure (see appendix). Another thing to note is the increase in the forward and reverse transformation stress for NiTi with increasing loading frequency. The increased change is significantly pronounced when the frequency is increased from 0.01 Hz to 1 Hz and not as pronounced in the 1 Hz to 10 Hz frequency range. However, for FeMnAlNi, the transformation stresses remain constant. Additionally, upon transformation, the sample exhibits considerable hardening which is apparent in Fig. 4b and c for NiTi at higher frequencies. The hardening is not significant for FeMnAlNi. The hardening rate increases notably from 0.01 Hz to 1 Hz for NiTi and remains constant thereafter. To rationalize the observed trends in the stress–strain behavior, the temperature evolution of the sample was extracted from IR thermography measurements. These results are presented in the next section.

Frequency Effects on the Temperature Evolution

The temperature evolution on the sample surface was monitored using IR thermography. Dual camera setup was employed to record optical images (for DIC strain measurements) and IR images (for temperature measurements) simultaneously in real time. Figure 5 depicts the temperature evolution with loading frequency. It is evident that the temperature change (ΔT) measured on the sample's surface increases with the loading frequency as the heat transfer into the ambient atmosphere is minimized. The temperature measurements were extracted from the sample's local area of interest (AOI) like that in Figs. 2 and 3. The ΔT was calculated as the difference between the sample's temperature prior to loading (i.e., RT) and the temperature at maximum applied displacement (strain) as shown in Fig. 6. Furthermore, the local ΔT increases with increasing local reversible strains as it is proportional to transformation strains and hence the transformed volume. Note that the transforming domain nucleates from a local region within the sample and sweeps the sample as the applied

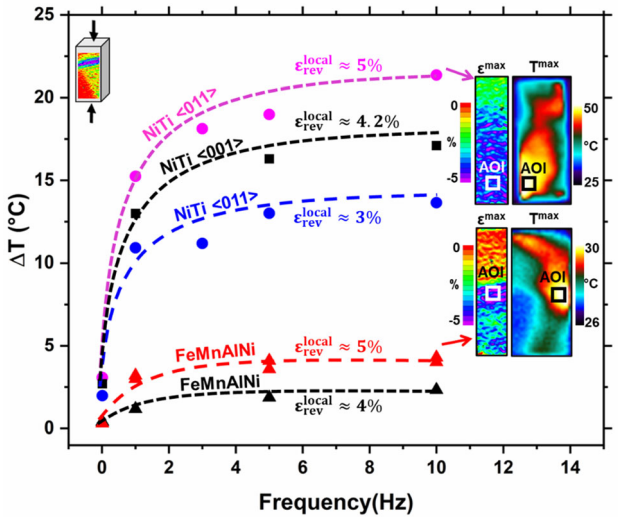

Fig. 5 Temperature evolution in the local AOI plotted against loading frequency at various local transformation strain magnitudes for all the loading orientations of NiTi and FeMnAlNi. Note the increase in ΔT with respect to loading frequency and the local reversible strains. Inset features the DIC and IR images, taken at peak strain, of NiTi $< 011 >$ and FeMnAlNi $< 123 >$ loaded at 10 Hz frequency. ΔT was measured as shown in Fig. 6 i.e. the difference between the temperature before loading (i.e. RT) and the temperature at peak strain

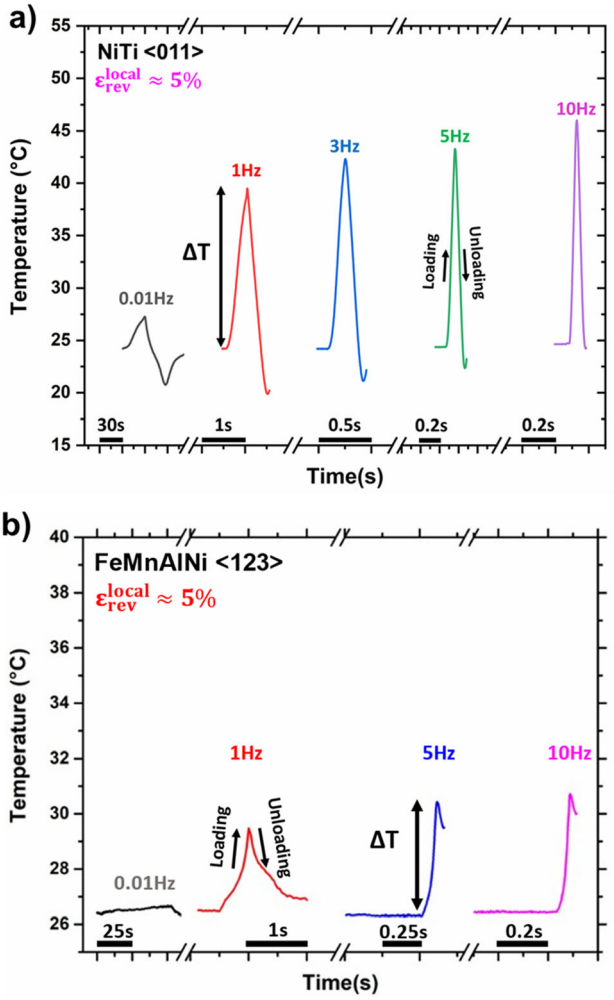

Fig. 6 Representative temperature vs time plot for **a** NiTi $< 011 >$ and **b** FeMnAlNi $< 123 >$. Note the difference in the scale of the temperature axis for NiTi and FeMnAlNi. The loading portion ends at the peak temperature for each loading frequency and the unloading portion commences. Refer the main text on the discussion about the asymmetry in the temperature evolution

strains are increased. Thus, initially the latent heat evolution is also concentrated in a local transforming domain. The volume swept by the transforming domain depends on the mobility of the A/M interface. Observing the temperature vs time plots in Fig. 6, one can see that the temperature evolution during loading and unloading is not symmetric. For example, for NiTi (Fig. 6a) the undercooling, due to the endothermic nature of the reverse transformation, below RT becomes progressively lower as the loading frequency is increased. As the loading frequency reaches 10 Hz and higher, the temperature evolution becomes more and more symmetric. This is reflected in the hysteresis vs frequency curves (Fig. 4a) as the loading frequency increases the hysteresis approaches a stabilized value. On the other hand, examining the temperature vs time curves for FeMnAlNi (Fig. 6b) one can see that the sample never undercools below RT. The magnitude of cooling achieved during the reverse transformation is lower than the heating. The possible origins of this is discussed in Frequency dependence of the stress–strain response.

Modeling Methodology and Results

An analytical thermomechanical model is employed following [72–74]. Only key elements of the model are described here, and the reader is referred to the aforementioned works for a more detailed exposition. In this framework, we consider the complimentary free energy $\Psi(\sigma_{ij}, T, f)$ as a function of the three-dimensional applied stress state σ_{ij}, the temperature of the sample T and the volume fraction of martensite f. For convenience, the model accounts for the nucleation and growth of only one martensitic variant in the austenite matrix. The total complimentary free energy at a given point can be expressed as,

$$\Psi(\sigma_{ij}, T, f) = \Delta G_{\text{chem}}(T, f) + W_{\text{elastic}}(\sigma_{ij}, f) + \sigma_{ij}\varepsilon_{ij} \quad (1)$$

where ΔG_{chem} is the chemical energy difference between the martensite and austenite phase, W_{elastic} constitutes the self-energy of a transformed martensitic inclusion inside an austenite matrix and the interaction energy between the transformed volume and applied load, and ε_{ij} is the macroscopic strain in the sample making the last term the

externally applied work in the sample. The chemical energy arises from a difference in bonding energy between the martensite and austenite phases and can be conveniently expressed as $\Delta G_{\text{chem}} = B(T_0 - T)f$ where B is proportional to the Clausius-Clapeyron slope of the SMA and T_0 is the equilibrium temperature of the austenite and martensite phases, both of which are intrinsic material parameters for the SMA. The elastic energy term can be derived as $W_{\text{elastic}} = \sigma_{ij}\varepsilon_{ij}^{\text{tr}} f + \frac{1}{2} f(1-f)\varepsilon_{ij}^{tr}[C_{ijkl}(S_{klmn}\varepsilon_{mn}^{tr} - \varepsilon_{mn}^{tr})]$ where $\varepsilon_{ij}^{\text{tr}}$ is the transformation strain corresponding to the nucleated variant of martensite, C is the elastic constant tensor and S is the Eshelby-tensor for the nucleated martensitic inclusion.

Starting from the austenite phase ($f = 0$), as increasing strain is applied to the material. The response remains linear-elastic, until a critical point is reached where $\frac{\partial \Psi}{\partial f}\Big|_{f=0} = F(0) = F_c$, with F_c as the critical driving force for the transformation. This driving force corresponds to barriers associated with the lattice friction of the transformation front and is hence an intrinsic material parameter. At this point A (Fig. 7a), martensitic transformation initiates and the corresponding level of stress is the critical transformation stress σ_{ij}^{tr}. Hence, this critical transformation stress is derived by solving for the stress in the following equation:

$$F_C = F(f=0) = B(T_0 - T) + \sigma_{ij}^{tr}\varepsilon_{ij}^{tr} + \frac{1}{2}\varepsilon_{ij}^{tr}[C_{ijkl}(S_{klmn}\varepsilon_{mn}^{tr} - \varepsilon_{mn}^{tr})] \quad (2)$$

In the transformation regime, the consistency condition is used to determine the mechanical response. This condition is given by $\Delta F = \frac{\partial F}{\partial f}\Delta f + \frac{\partial F}{\partial \sigma} : \Delta\sigma + \frac{\partial F}{\partial T}\Delta T = 0$, which can be derived as:

$$B(-\Delta T) + (\Delta\sigma_{ij})\varepsilon_{ij}^{tr} - \Delta f \varepsilon_{ij}^{tr}[C_{ijkl}(S_{klmn}\varepsilon_{mn}^{tr} - \varepsilon_{mn}^{tr})] = 0 \quad (3)$$

Note that we allow a temperature change during the transformation phase, given by ΔT. This temperature change accounts for the heating of the sample during the exothermic forward transformation. The measured temperature change from the IR thermography is incorporated. Equation (3) is employed to determine the final volume fraction $\Delta f = f^{\max}$ of martensite corresponding to the maximum applied strain at the end of the transformation i.e. $\varepsilon = \varepsilon_{\max}$ at B (Fig. 7a). Then upon unload, the material unloads elastically until the critical point for reverse transformation is reached (point C in Fig. 7a), characterized by $-\frac{\partial \Psi}{\partial f}\Big|_{f=f^{\max}} = -F(f^{\max}) = F_c$. At this point, reverse transformation initiates and the consistency condition (3) is employed until the volume fraction f reduces to zero till point D (Fig. 7a). At this point, reverse transformation is complete, shifting the unloading to an elastic process once more. In this manner, the entire superelastic mechanical response can be modeled to predict the energy dissipated (hysteresis) within the stress–strain curve.

The nucleated martensite inside the austenitic matrix is modeled as a penny-shaped inclusion with an aspect ratio $a_2/a_1 = 1.0\text{E}-4$. The Eshelby tensor corresponding to this geometry can be obtained from [76]. The material constants employed for NiTi are taken from [73, 77]. It must be noted that these constants were obtained from experiments on polycrystalline NiTi but are quite effective for the spirit in which this model is employed. The model is applied for [011]-compression of NiTi, considering the martensitic variant with the highest Schmid factor to be nucleated (out of all variants listed in [73] for NiTi). The temperature change during the transformation, i.e. ΔT is obtained from experiment (Fig. 6). For the purposes of the model it is assumed that the temperature change in the forward and reverse transformation are equal and opposite. The prediction of the normalized hysteresis at different frequencies captures the trend in experimental data well, as seen in Fig. 7b. For FeMnAlNi, it must be realized that material constants suitable for the thermomechanical model are still unavailable as this SMA is relatively new. We approach its behavior by making the fewest parametric changes from the baseline values chosen thereby identifying the key material parameter influencing frequency-sensitivity. We only change the parameter B, which is proportional to the Clausius-Clapeyron slope of the SMA. Once B is reduced by half, the experimental trend is explained very well (Fig. 7b). See appendix for the experimental Clausius-Clapeyron plots of FeMnAlNi and NiTi reported in the literature.

Discussion

Damping Capacity of Shape Memory Alloys

Elegant and minimal solutions to various problems in modern day engineering can be sought using SMAs. Damping of resonant frequencies in an earthquake resistant structure, during re-entry/take-off of space crafts, self-stabilizing robotics, and micro electro mechanical system (MEMS) devices are some of the problems that warrant the use of SMAs [1, 78, 79]. It is well known that the martensitic phase in SMAs has a higher specific damping capacity compared to austenite phase due to the internally twinned structure. However, in the temperatures where martensite and austenite can co-exist, the specific damping capacity is the highest due to the presence of an additional interface, the austenite–martensite interface. The standard

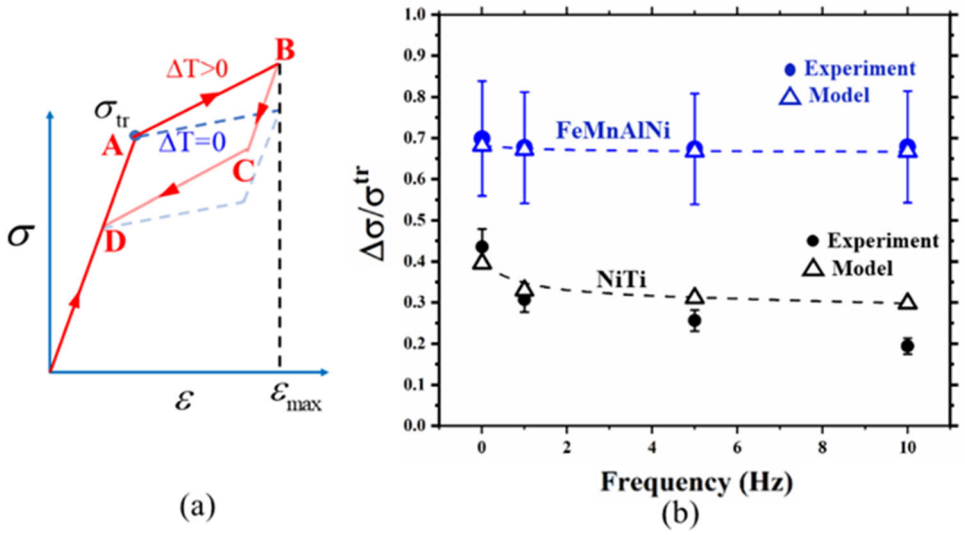

Fig. 7 **a** Thermomechanical modeling of the superelastic response (Modeling methodology and results); the critical points of the transformation (A, B, C, D) are marked along with the critical transformation stress σ_{tr} and the maximum applied strain ε_{max}; The curve in red depicts the curve when there is a temperature change of the sample during the forward/reverse transformations, while the blue curve represents the response when there is no temperature change in the sample; for the model, the temperature change during transformation is obtained from experiment **b** comparison of estimates of normalized hysteresis from the thermomechanical model and experiment; the parameters chosen for the model are for NiTi ((B = 0.607 MPa/K, F_c = 5.4 MPa, $T_o = -9.2\,^{o}C$ G = 28 GPa, ν = 0.4 [73, 77]) showing good agreement with experiments; the behavior of FeMnAlNi is well-reproduced by one parametric change i.e. reduction of the parameter B (in this case, by a factor of 2) representative of the Clausius-Clapeyron slope (Color figure online)

internal friction tests conducted during heating/cooling using a torsion pendulum setup have elucidated the different contributions to the internal friction as the transitory part, the phase transformation part, and the intrinsic part [14, 19, 43]. However, the contribution of the different mechanisms for a superelastic deformation is of interest in this study and is discussed further.

Frequency Dependence of the Stress–strain Response

As presented in Fig. 4, the stress hysteresis is loading frequency dependent for NiTi. The latent heat release during the forward transformation heats the sample. As depicted in Fig. 5, the corresponding ΔT is higher at increasing frequencies as heat transfer is minimized into the ambient atmosphere during the time period of the test. It is known that the M_s, M_f, A_s and A_f temperatures increase with the application of external stress [80, 81]. Thermodynamic models which take into account the elastic and chemical contributions to the overall free energy of the system show that the externally applied stress field assists the forward transformation as the Gibbs free energy difference between the martensitic and the austenitic states gets maximized [73, 82]. The temperature rise during the forward transformation decreases the chemical free energy difference between the austenite and martensite phase and thus the stress needs to be increased to sustain the forward transformation which gives rise to hardening. However, the temperature rise during loading provides a driving force for reverse transformation during unloading and the martensite to austenite transformation occurs at a higher stress. Effectively the area under the hysteresis loop decreases. This can be interpreted as a decrease in the transitory contribution to the total internal friction. The heating during the forward transformation assists the mobility of the A/M interface during the reverse transformation (Fig. 8a). For NiTi, one can see from Fig. 6a, that the magnitude of heating during loading is lesser than the magnitude of cooling during unloading at lower frequencies. In other words, the rate of change of temperature is asymmetric with respect to loading/unloading rate. As the loading rate is increased, the temperature rate approaches a symmetric behavior (compare 0.01 Hz and 10 Hz in Fig. 6a). The corresponding ΔT approaches a steady state (Fig. 5). Hence the change in stress hysteresis and the transitory contribution to the total IF also approach a steady state above 10 Hz. This is also elucidated by the modeling results presented in Modeling methodology and results (Fig. 7). Additionally, in the superelastic deformation, the mobility of the internally twinned martensite needs to be accounted for as well. The difference between the mobilities of the A/M interface and the twin interface is expected to affect the damping capacity [42]. This can be interpreted in terms of the mechanism of the phase transformation which would influence the phase transformation part of the internal friction.

The mobility of the internal twin boundary (TB) is achieved by the motion of partial dislocations residing on the TB [83, 84]. The mobility of the partials would in turn depend on the elastic modulus of the martensite phase, the magnitude of the resolved shear stress on the TB, twin migration energy, the frictional resistance to the partial motion, partial density, burgers vector, and amplitude of motion. All of which depend on the martensite variant that gets activated based on the local stress state. Further, the twin partial density is impacted by the elastic strains sustained by the activated martensite variant in response to the stress state [85]. This local stress state is in turn affected by the precipitate structure, defect density and loading orientation. The mobility of the A/M interface depends on the interface energy, the elastic distortion at the boundary and the resulting coherency strains. Lower the coherency strains, higher the mobility of the A/M interface. The coherency strains in turn depend on the crystal structures of the austenite, martensite and the respective twin thickness of the internally twinned martensite [48, 52, 86, 87]. Consequently, based on the relative mobilities of the A/M interface and the internal TB, a dislocation reaction may occur when the twin partials encounter a barrier such as the A/M interface resulting in dislocation emission into the austenite matrix [51, 53] and thus contributing towards energy dissipation. Additionally, depending on the magnitude of the coherency strains at the A/M interface and the loading orientation, relaxation of coherency strains may

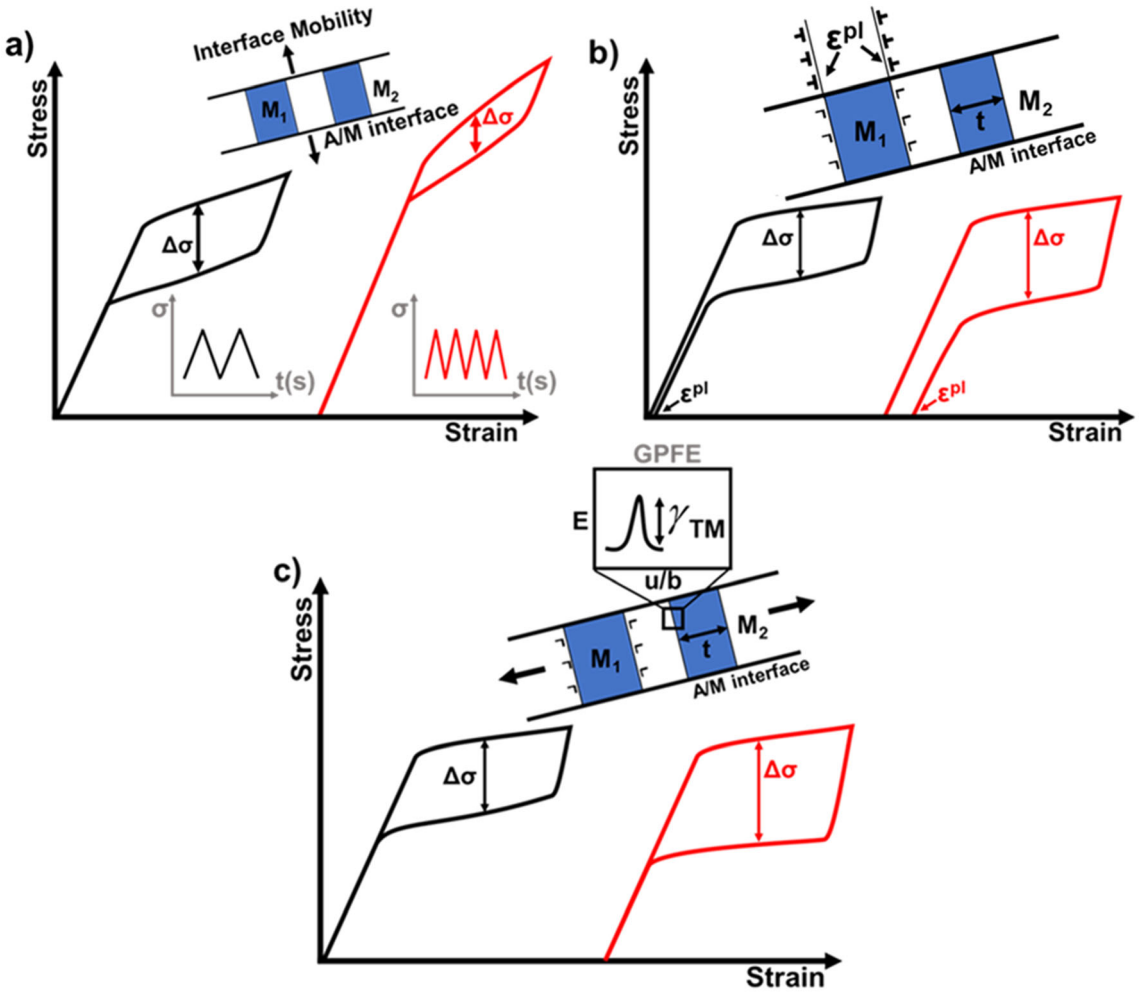

Fig. 8 A schematic elucidating the different mechanisms behind the damping capacity of SMAs. **a** Transitory part of the internal friction. It depends on the kinetics of phase transformation such as the rate of evolution of martensite, self-heating/cooling rate, and the magnitude of change in temperature all of which affects the frictional resistance of the A/M interface. **b** Phase transformation part of the internal friction which mainly accounts for the plastic dissipation at the A/M interface. It is governed by the mechanism of phase transformation which dictates the twin thickness (t) of the internally twinned martensite, coherency strains at the A/M interface and consequently the slip emission. **c** Intrinsic part of the internal friction which accounts for the intrinsic damping capacity of the internally twinned martensite and the austenite. Damping capacity of martensite is governed by the twin interface density, hence the twin thickness (t), the twin migration energy and the consequent frictional resistance to the motion of twinning partials. For the austenite, damping capacity stems from the motion of vacancies, matrix dislocations and is negligible compared to that of martensite (Color figure online)

occur when the interface traverses precipitates or in-grown dislocations resulting in plastic dissipation [46–48, 54]. The effect of loading orientation is reflected in the difference in the hysteresis of NiTi $< 011 >$ and $< 001 >$ orientations. The lower hysteresis for $< 001 >$ is due to the absence of plastic dissipation as the resolved shear stress on the most energetically favorable slip system $(011) < 001 >$ [82, 88] is zero. Thus the phase transformation part of the internal friction which is thought to arise from dislocation relaxation processes [44], is absent in NiTi $< 001 >$. However, the transitory contribution seems to be present for NiTi $< 001 >$ and the decrease in the hysteresis with frequency reflects that.

On the other hand, FeMnAlNi exhibits rate insensitive behavior. The hysteresis remains fairly constant with increasing frequency and can be attributed to the temperature independent superelastic response of FeMnAlNi. FeMnAlNi exhibits a Clausius-Clapeyron slope of 0.2 to 0.6 MPa/°C [57, 89, 90] (Fig. 12) owing to the extremely low magnitudes of ΔS (≈ -0.4 J/mol/K) of phase transformation [59]. The maximum ΔT measured is almost 5 times lower than that of NiTi. Looking at Fig. 6b, it can be noted ΔT measured at 0.01 Hz is negligible (≈ 0.3 °C) for FeMnAlNi, whereas for NiTi ΔT at 0.01 Hz is around 3 °C (ten times more). At increasing frequencies maximum ΔT measured is around 4 °C at 10 Hz, however, contrasting to NiTi, the latent heat absorption during reverse transformation is not enough to cool the sample back to RT. This suggests that the magnitude of latent heat release during forward transformation is higher than that absorbed during reverse transformation. However, one should note that the heat transfer into the ambient atmosphere could play a part in the dissimilarity of ΔT during forward and reverse transformation, but prior studies [91] have indeed observed different magnitudes of latent heat during forward and reverse transformation in a DSC test. Another explanation could be that most of the heating during loading stems from plastic dissipation and is irreversible. The latter explanation seems more feasible as the latent heat of transformation is negligible for FeMnAlNi as inferred from the extremely low ΔS reported [59]. The propensity for slip in FeMnAlNi is further discussed in the next paragraph. Furthermore, the results from the thermomechanical model in Modeling methodology and results show that, in addition to the lower temperature change, the material parameter which ultimately dictates frequency-sensitivity is the Clausius-Clapeyron slope. This slope not only depends on the latent heat of transformation (or entropy change) but also on the transformation strain [91, 92]. Hence, design of SMAs for damping applications must focus on minimizing this parameter and not only the latent heat.

It is also worth noting that, despite frequency-insensitivity, the magnitude of stress hysteresis (and specific damping capacity) is higher compared to that of NiTi. This can be attributed to the mechanism of phase transformation. FeMnAlNi has 3 lattice correspondences [93] compared to 12 for NiTi. NiTi undergoes a B2 to B19' phase transformation and FeMnAlNi undergoes a BCC to FCC transformation. Absence of a group-subgroup relationship for a BCC to FCC transformation [50] along with fewer lattice correspondences results in relaxation of the coherency strains in the A/M interface and plastic dissipation occurs. Thus, the contribution from the phase transformation part of the internal friction is higher for FeMnAlNi compared to NiTi. Additionally, to sustain larger coherency strains at the A/M interface, the internal twin thickness of FeMnAlNi is much lower compared to that of NiTi [90, 94] giving rise to high density of twin interfaces. This suggests that the intrinsic contribution of FeMnAlNi is also higher compared to NiTi. Higher specific damping capacity, rate insensitivity and temperature independent stress–strain response can be beneficial for various engineering applications. Nevertheless, the response under fatigue loading needs to be considered given the higher propensity for plastic dissipation in FeMnAlNi. Recent studies have shown that the degradation of functionality due to residual strain accumulation can be closely linked to structural failure via crack initiation and crack growth along the A/M interface [61, 95]. These issues need to be well understood especially for load bearing applications such as in earthquake resistant structures.

In summary, the transitory part of the internal friction is linked to the mobility of the A/M interface alone and the various factors that influence it (Fig. 8a). The phase transformation part of the internal friction is linked to the structure of the A/M interface, the internal TB of the martensite, their relative mobilities and the associated plastic dissipation mechanism (Fig. 8b). The intrinsic part of the internal friction depends on the mobility of the internal TB alone and does not account for plastic dissipation (Fig. 8c). These contributions need not be independent as the mobility of the A/M interface, the structure of the A/M interface, the structure of the internal twins and their mobility are related [48, 52, 87]. A change in one of the contributions could have a cascading effect and influence the other contributions as well.

Variability in FeMnAlNi

The specific damping capacity, which is the ratio of area under the hysteresis loop and the total applied strain energy, of FeMnAlNi and NiTi is shown in Fig. 9. Its variation with respect to the loading rate is same as that of normalized stress hysteresis presented in Fig. 4. The Clausius-Clapeyron plots for FeMnAlNi [57, 59, 89] and NiTi [96] shown in Fig. 12 portray the large variability in the transformation stress for FeMnAlNi as reported in the literature. Additionally, the

specific damping capacity of FeMnAlNi reported in this study shows large variability as well. This can be attributed to the initial microstructure. FeMnAlNi has high quench sensitivity, exhibits a dual FCC+BCC phase at room temperature and pure BCC (austenite) phase at the quenching temperature of 1300 °C. Any delay in quenching, even by a few seconds, can render the as-quenched microstructure with some martensite. Additionally, upon quenching from a temperature of 1300 °C the high thermal stresses could also render the microstructure with an initial volume fraction of martensite. As one can see in Fig. 9, for the same orientation, the initial microstructure (see optical and SEM images) is completely different even though the heat treatment procedure is the same. It is known that this alloy system is extremely sensitive to the characteristics of the precipitates [89] which influence the stress levels of the forward/reverse transformation. Additionally it was recently shown that the growth of precipitates is impeded in FCC martensite compared to that in BCC austenite [97]. Thus, the initial microstructure prior to ageing is expected to affect the precipitate volume fraction and size in the local regions of the sample. The complex internal stress field generated by the different habit plane variants of the quenching-induced martensite and the inhomogeneity in the precipitate volume fraction/size in the local regions of the sample will influence the stress levels of the transformation and hence the hysteresis. On the other hand, comparing the stress–strain curves of two different samples of NiTi with the same loading orientation (Fig. 11), it is evident that the variability in specific damping capacity is minimal.

Conclusions

In the present study, rate sensitivity of two starkly contrasting SMA systems namely $Ni_{50.8}Ti$ and $Fe_{43.5}Mn_{34}Al_{15}Ni_{7.5}$ single crystals were tested in the superelastic regime. In the wake of the experimental results and the modeling efforts, the following conclusions can be drawn,

1. NiTi is highly rate sensitive owing to its relatively large ΔT during loading. The large ΔT can be attributed to the correspondingly large ΔS during the austenite to martensite transformation. On the other hand, FeMnAlNi exhibited rate insensitive stress–strain response due to its relatively low ΔT during loading.
2. Along with the experiments, the thermodynamic model revealed that the key material parameter that dictates rate sensitivity in superelastic SMA is the Clausius-Clapeyron slope.
3. The decrease in the stress hysteresis and the specific damping capacity with loading frequency could be attributed to the decrease in the transitory part of the IF which accounts for the mobility and the frictional resistance of the A/M interface.
4. The magnitude of normalized stress hysteresis and the specific damping capacity is lower for NiTi $< 001 >$ loading orientation compared to that of NiTi $< 011 >$. This could be ascribed to negligible contribution from the phase transformation part of the IF which accounts for plastic dissipation. In NiTi $< 001 >$, the resolved shear stress factor on the most favorable slip system $(011) < 001 >$ is zero and hence no transformation induced plasticity at the A/M interface.
5. Comparing between NiTi and FeMnAlNi, FeMnAlNi exhibits a higher magnitude of normalized stress hysteresis and specific damping capacity. This could be attributed to a relatively larger contribution from the phase transformation part and the intrinsic part of the IF. Thus, it can be said that FeMnAlNi SMA has a higher propensity for inelastic strain accumulation during a load/unload cycle and will have implications in fatigue loading.
6. High variability noted in FeMnAlNi could be attributed to the variability in the initial quenched microstructure. Following the exact same heat treatment procedure for all the samples, high thermal stresses due to quenching from 1300 °C renders the microstructure with an initial volume fraction of martensite. This affects the ageing mechanism in the subsequent step and eventually influences the stress levels during forward/reverse transformation thereby giving rise to variability.

Thus, it can be concluded that FeMnAlNi SMA could be an impressive candidate for damping applications due to its rate insensitive behavior, near-zero temperature dependence of the superelastic response and a higher specific damping capacity.

Acknowledgements This work is supported by the National Science Foundation DMR Grant 1709515 Metallic Materials and Nanomaterials Program which is gratefully acknowledged. We would like to thank Prof. Yuri Chumlyakov of Tomsk State University, Russia for providing the single crystals. SEM and EBSD were carried out in part in the Frederick Seitz Materials Research Laboratory Central Research Facilities, University of Illinois Urbana-Champaign.

Appendix

Specific Damping Capacity, Sample Variability and Clausius-Clapeyron Slope

The specific damping capacity, which is the ratio of area under the hysteresis loop and the total applied strain energy, of FeMnAlNi and NiTi is shown in Fig. 9 below.

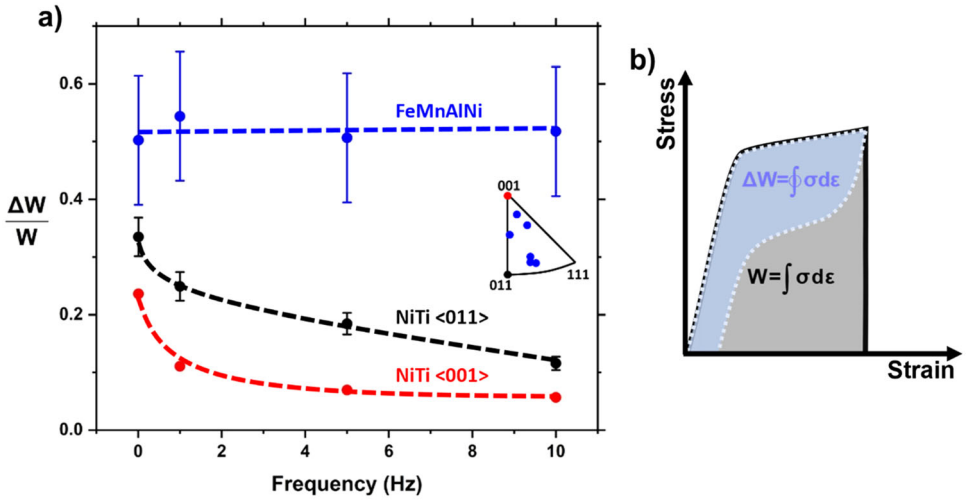

Fig. 9 **a** Specific damping capacity vs loading frequency for NiTi and FeMnAlNi single crystals. **b** Schematic depicting stored elastic strain energy (W) and dissipated energy (ΔW)

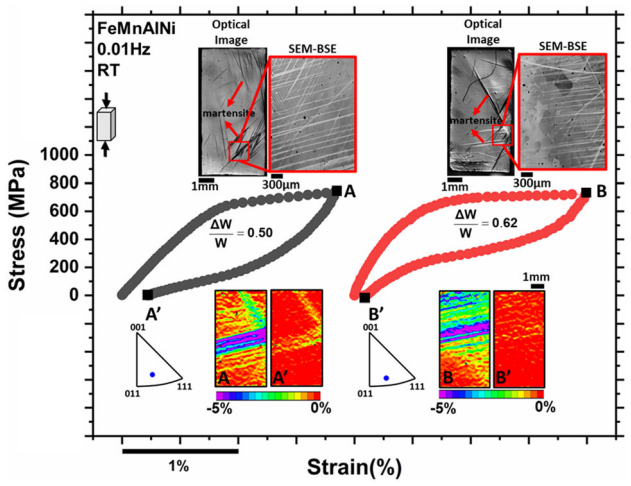

Fig. 10 Stress–Strain behavior of two FeMnAlNi samples with near < 123 > orientation and different initial microstructure. Note the values of specific damping capacity. DIC insets depict only one dominant variant is active for both the samples. Just by visual inspection, AA' seems to have higher initial martensite volume fraction

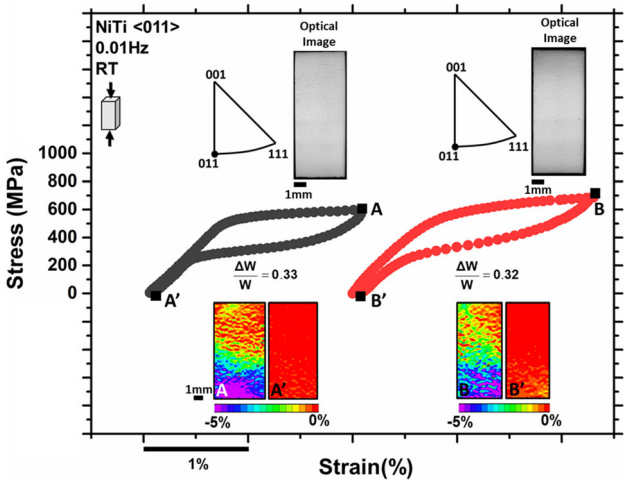

Fig. 11 Stress–Strain behavior of two NiTi samples with < 011 > loading orientation and similar initial microstructure

Figure 10 depicts the stress strain curves of two different FeMnAlNi samples with near < 123 > orientation and different initial microstructure, note the variability in the stress–strain behavior and the specific damping capacity. Figure 11 depicts the stress strain curves of two different NiTi samples with < 011 > loading orientation and same initial microstructure having nearly the same specific damping capacity.

Variation of transformation stress with loading temperature for FeMnAlNi and NiTi are shown in Fig. 12. The data were collected from prior studies. Note the wide range of superelastic functionality for FeMnAlNi, all the way from −196 °C to at least 240 °C. The Clausius-Clapeyron

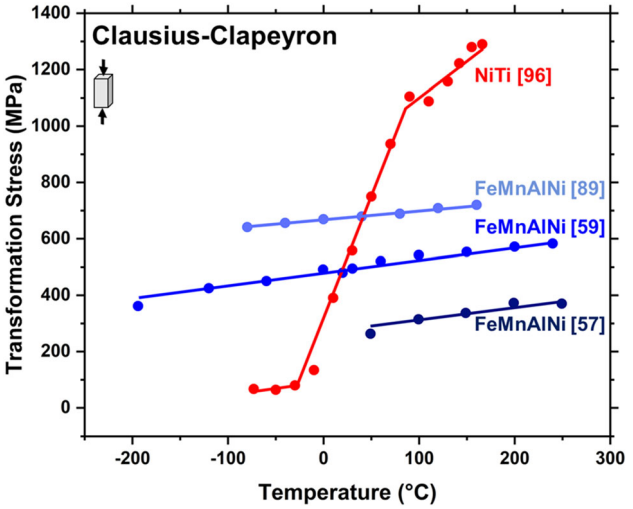

Fig. 12 Compressive transformation stress vs temperature for FeMnAlNi [57, 59, 89] and NiTi [96] single crystals

slope ranges from 0.2 to 0.6 MPa/°C. The wide range of variability in the transformation stresses can be attributed to different ageing times resulting in different precipitate sizes. The FeMnAlNi shown in Fig. 12 were aged at 200 °C for 3 h [57], 24 h [59] and 10 h [89]. Whereas, for $Ni_{50.8}Ti$ with an ageing time of 1.5 h at 550 °C, the superelastic functionality is limited to a temperature range of about 0–90 °C [97]. The Clausius-Clapeyron slope ranges from 7 to 10 MPa/°C.

References

1. Otsuka K, Wayman CM (1999) Shape memory materials. Cambridge University Press, Cambridge
2. Hartl DJ, Lagoudas DC (2007) Aerospace applications of shape memory alloys. Proc Ins Mech Eng G 221(4):535–552
3. Janke L, Czaderski C, Motavalli M, Ruth J (2005) Applications of shape memory alloys in civil engineering structures—overview, limits and new ideas. Mater Struct 38(5):578–592
4. Safranski D, Dupont K, Gall K (2020) Pseudoelastic NiTiNOL in Orthopaedic Applications. Shape Memory and Superelasticity 6(3):332–341
5. Song S-H, Lee J-Y, Rodrigue H, Choi I-S, Kang YJ, Ahn S-H (2016) 35 Hz shape memory alloy actuator with bending-twisting mode. Sci Rep 6:21118
6. Duerig TW (2002) The use of superelasticity in modern medicine. MRS Bull 27(2):101–104
7. Torra V, Martorell F, Lovey FC, Sade ML (2017) Civil engineering applications: specific properties of NiTi thick wires and their damping capabilities. a review. Shap Mem Superelasticity 3(4):403–413
8. Williams EA, Shaw G, Elahinia M (2010) Control of an automotive shape memory alloy mirror actuator. Mechatronics 20(5):527–534
9. Karaman I, Basaran B, Karaca HE, Karsilayan AI, Chumlyakov YI (2007) Energy harvesting using martensite variant reorientation mechanism in a NiMnGa magnetic shape memory alloy. Appl Phys Lett 90(17):172505
10. Pagounis E, Muellner P (2018) materials and actuator solutions for advanced magnetic shape memory devices, ACTUATOR 2018; 16th International Conference on New Actuators, pp. 1–7
11. Bucsek AN, Nunn W, Jalan B, James RD (2020) energy conversion by phase transformation in the small-temperature-difference regime. Annu Rev Mater Res 50:283–318
12. Müller I, Xu H (1991) On the pseudo-elastic hysteresis. Acta Metall Mater 39(3):263–271
13. Blanter MS, Golovin IS, Neuhäuser H, Sinning H-R (2007) Other mechanisms of internal friction, internal friction in metallic materials: a handbook. Springer, Berlin Heidelberg, pp 121–155
14. San Juan J, Nó M (2003) Damping behavior during martensitic transformation in shape memory alloys. J alloys compds 355(1–2):65–71
15. Van Humbeeck J (2001) 5.3 the martensitic transformation. Mater Sci Forum 366–368:382–415
16. Kumar PK, Lagoudas DC (2008) Introduction to shape memory alloys, shape memory alloys: modeling and engineering applications. Springer, Boston, pp 1–51
17. Juan JS, Nó ML, Schuh CA (2009) Nanoscale shape-memory alloys for ultrahigh mechanical damping. Nat Nanotechnol 4(7):415–419
18. Bidaux J-E, Schaller R, Benoit W (1989) Study of the hcp-fcc phase transition in cobalt by acoustic measurements. Acta Metall 37(3):803–811
19. San Juan J, Perez-Saez RB (2001) 5.4 transitory effects. Mater Sci Forum 366–368:416–436
20. Van Humbeeck J (2003) Damping capacity of thermoelastic martensite in shape memory alloys. J Alloy Compd 355(1):58–64
21. Segui C, Cesari E, Pons J, Chernenko V (2004) Internal friction behaviour of Ni–Mn–Ga. Mater Sci Eng A 370(1):481–484
22. Chen Y, Jiang HC, Liu SW, Rong LJ, Zhao XQ (2009) Damping capacity of TiNi-based shape memory alloys. J Alloy Compd 482(1):151–154
23. He Y, Yin H, Zhou R, Sun Q (2010) Ambient effect on damping peak of NiTi shape memory alloy. Mater Lett 64(13):1483–1486
24. Dayananda GN, Rao MS (2008) Effect of strain rate on properties of superelastic NiTi thin wires. Mater Sci Eng A 486(1):96–103
25. Dolce M, Cardone D (2001) Mechanical behaviour of shape memory alloys for seismic applications 2. Austenite NiTi wires subjected to tension. int J Mech Sci 43(11):2657–2677
26. DesRoches R, McCormick J, Delemont M (2004) Cyclic properties of superelastic shape memory alloy wires and bars. J Struct Eng 130(1):38–46
27. Nemat-Nasser S, Yong Choi J, Guo W-G, Isaacs JB, Taya M (2005) High strain-rate, small strain response of a NiTi shape-memory alloy. J Eng Mater Technol 127(1):83–89
28. Malécot P, Lexcellent C, Foltête E, Collet M (2006) Shape memory alloys cyclic behavior: experimental study and modeling. J Eng Mater Technol 128(3):335–345
29. Tobushi H, Shimeno Y, Hachisuka T, Tanaka K (1998) Influence of strain rate on superelastic properties of TiNi shape memory alloy. Mech Mater 30(2):141–150
30. Heller L, Šittner P, Pilch J, Landa M (2009) Factors controlling superelastic damping capacity of SMAs. J Mater Eng Perform 18(5):603–611
31. Yin H, He Y, Sun Q (2014) Effect of deformation frequency on temperature and stress oscillations in cyclic phase transition of NiTi shape memory alloy. J Mech Phys Solids 67:100–128
32. Zhang X, Feng P, He Y, Yu T, Sun Q (2010) Experimental study on rate dependence of macroscopic domain and stress hysteresis in NiTi shape memory alloy strips. Int J Mech Sci 52(12):1660–1670
33. Van Humbeeck J, Delaey L (1981) THE influence of strain-rate, amplitude and temperature on the hysteresis of a pseudoelastic Cu-Zn-Al single crystal. J Phys Colloques 42(C5):C5-1007-C5-1011
34. Hartl DJ, Lagoudas DC (2008) Thermomechanical characterization of shape memory alloy materials, shape memory alloys: modeling and engineering applications. Springer, Boston, pp 53–119
35. Leo PH, Shield TW, Bruno OP (1993) Transient heat transfer effects on the pseudoelastic behavior of shape-memory wires. Acta Metall Mater 41(8):2477–2485
36. Shaw JA, Kyriakides S (1995) Thermomechanical aspects of NiTi. J Mech Phys Solids 43(8):1243–1281
37. Yin H, Yan Y, Huo Y, Sun Q (2013) Rate dependent damping of single crystal CuAlNi shape memory alloy. Mater Lett 109:287–290
38. Zener C (1938) Internal friction in solids II. General theory of thermoelastic internal friction. Phys Rev 53(1):90
39. Moumni Z, Herpen AV, Riberty P (2005) Fatigue analysis of shape memory alloys: energy approach. Smart Mater Struct 14(5):S287–S292
40. Sateesh VL, Senthilkumar P, Satisha, Dayananda GN (2014) Low Cycle fatigue evaluation of NiTi SESMA thin wires. J Mater Eng Perform 23(7):2429–2436

41. Zhang Y, You Y, Moumni Z, Anlas G, Zhu J, Zhang W (2017) Experimental and theoretical investigation of the frequency effect on low cycle fatigue of shape memory alloys. Int J Plast 90:1–30
42. Dejonghe W, Batist D (1976) Factors affecting the internal friction peak due to thermoelastic martensitic transformation. Scripta Metallurgica 10:1125–1128
43. Perez-Saez R, Recarte V, Nó M, San Juan J (1998) Anelastic contributions and transformed volume fraction during thermoelastic martensitic transformations. Phys Rev B 57(10):5684
44. Mercier O, Melton K (1976) The influence of an anisotrophic elastic medium on the motion of dislocations: application to the martensitic transformation. Scr Metall 10(12):1075–1080
45. Hornbogen E (1985) The effect of variables on martensitic transformation temperatures. Acta Metall 33(4):595–601
46. Hornbogen E (2004) Review thermo-mechanical fatigue of shape memory alloys. J Mater Sci 39(2):385–399
47. Olson G, Cohen M (1975) Thermoelastic behavior in martensitic transformations. Scr Metall 9(11):1247–1254
48. Roitburd A, Kurdjumov G (1979) The nature of martensitic transformations. Mater Sci Eng 39(2):141–167
49. Bhattacharya K (2003) Microstructure of martensite: why it forms and how it gives rise to the shape-memory effect. Oxford University Press, Oxford
50. Bhattacharya K, Conti S, Zanzotto G, Zimmer J (2004) Crystal symmetry and the reversibility of martensitic transformations. Nature 428(6978):55
51. Kajiwara S (1999) Characteristic features of shape memory effect and related transformation behavior in Fe-based alloys. Mater Sci Eng A 273–275:67–88
52. Kajiwara S, Owen WS (1977) The martensite-austenite interface and the thickness of twins in martensite in Fe3Pt. Scr Metall 11(2):137–142
53. Mohammed ASK, Sehitoglu H (2020) Martensitic twin boundary migration as a source of irreversible slip in shape memory alloys. Acta Mater 186:50–67
54. Simon T, Kröger A, Somsen C, Dlouhy A, Eggeler G (2010) On the multiplication of dislocations during martensitic transformations in NiTi shape memory alloys. Acta Mater 58(5):1850–1860
55. Humbeeck JV, Kustov S (2005) Active and passive damping of noise and vibrations through shape memory alloys: applications and mechanisms. Smart Mater Struct 14(5):S171–S185
56. Vollmer M, Krooß P, Karaman I, Niendorf T (2017) On the effect of titanium on quenching sensitivity and pseudoelastic response in Fe-Mn-Al-Ni-base shape memory alloy. Scripta Mater 126:20–23
57. Abuzaid W, Wu Y, Sidharth R, Brenne F, Alkan S, Vollmer M, Krooß P, Niendorf T, Sehitoglu H (2019) FeMnNiAl iron-based shape memory alloy: promises and challenges. Shap Mem Superelasticity 5:263–277
58. Xia J, Noguchi Y, Xu X, Odaira T, Kimura Y, Nagasako M, Omori T, Kainuma R (2020) Iron-based superelastic alloys with near-constant critical stress temperature dependence. Science 369(6505):855–858
59. Omori T, Ando K, Okano M, Xu X, Tanaka Y, Ohnuma I, Kainuma R, Ishida K (2011) Superelastic effect in polycrystalline ferrous alloys. Science 333(6038):68–71
60. Vollmer M, Baunack D, Janoschka D, Niendorf T (2020) Induction butt welding followed by abnormal grain growth: a promising route for joining of Fe–Mn–Al–Ni tubes. Shap Mem Superelasticity. 6:131–138
61. Sidharth R, Wu Y, Brenne F, Abuzaid W, Sehitoglu H (2020) Relationship between functional fatigue and structural fatigue of iron-based shape memory alloy FeMnNiAl. Shap Mem Superelasticity. 6:256–272
62. Van Humbeeck J (2001) Shape memory alloys: a material and a technology. Adv Eng Mater 3(11):837–850
63. Otsuka K, Ren X (2005) Physical metallurgy of Ti–Ni-based shape memory alloys. Prog Mater Sci 50(5):511–678
64. Calvi A (2011) Spacecraft loads analysis. ESA/ESTEC, Noordwijk, The Netherlands
65. Torra V, Isalgue A, Lovey FC, Sade M (2015) Shape memory alloys as an effective tool to damp oscillations. J Therm Anal Calorim 119(3):1475–1533
66. Ahadi A, Sun Q (2013) Stress hysteresis and temperature dependence of phase transition stress in nanostructured NiTi—effects of grain size. Appl Phys Lett 103(2):021902
67. He YJ, Sun QP (2011) On non-monotonic rate dependence of stress hysteresis of superelastic shape memory alloy bars. Int J Solids Struct 48(11):1688–1695
68. He YJ, Sun QP (2011) Rate-dependent damping capacity of NiTi shape memory alloy. Solid State Phenom 172–174:37–42
69. Sun S, Rajapakse RKND (2003) Simulation of pseudoelastic behaviour of SMA under cyclic loading. Comput Mater Sci 28(3):663–674
70. Ikeda TJ (2015) Analytical investigation of strain loading frequency effect on stress-strain-temperature relationship of shape-memory alloy. Archiv Mech 67(4):275–291
71. Yu C, Kang G, Kan Q, Zhu Y (2015) Rate-dependent cyclic deformation of super-elastic NiTi shape memory alloy: thermo-mechanical coupled and physical mechanism-based constitutive model. Int J Plast 72:60–90
72. Huang M, Brinson LC (1998) A multivariant model for single crystal shape memory alloy behavior. J Mech Phys Solids 46(8):1379–1409
73. Gall K, Sehitoglu H (1999) The role of texture in tension–compression asymmetry in polycrystalline NiTi. Int J Plast 15(1):69–92
74. Hamilton RF, Sehitoglu H, Chumlyakov Y, Maier H (2004) Stress dependence of the hysteresis in single crystal NiTi alloys. Acta Mater 52(11):3383–3402
75. Omori T, Nagasako M, Okano M, Endo K, Kainuma R (2012) Microstructure and martensitic transformation in the Fe-Mn-Al-Ni shape memory alloy with B2-type coherent fine particles. Appl Phys Lett 101(23):231907
76. Mura T (1987) Isotropic inclusions. In: Mura T (ed) Micromechanics of defects in solids. Springer, Dordrecht, pp 74–128
77. Ren G, Sehitoglu H (2016) Interatomic potential for the NiTi alloy and its application. Comput Mater Sci 123:19–25
78. Lagoudas DC (2008) Shape memory alloys: modeling and engineering applications. Springer, Berlin
79. Duerig TW, Melton K, Stöckel D (2013) Engineering aspects of shape memory alloys. Butterworth-heinemann, Oxford
80. Tanaka K, Kobayashi S, Sato Y (1986) Thermomechanics of transformation pseudoelasticity and shape memory effect in alloys. Int J Plast 2(1):59–72
81. Liu Y, Galvin S (1997) Criteria for pseudoelasticity in near-equiatomic NiTi shape memory alloys. Acta Mater 45(11):4431–4439
82. Patoor E, El Amrani M, Eberhardt A, Berveiller M (1995) Determination of the origin for the dissymmetry observed between tensile and compression tests on shape memory alloys. Le Journal de Physique IV 5(C2):C2-495-C2-500
83. Hirth J, Wang J, Tomé C (2016) Disconnections and other defects associated with twin interfaces. Prog Mater Sci 83:417–471
84. Mohammed ASK, Sehitoglu H (2020) Modeling the interface structure of type II twin boundary in B19′ NiTi from an atomistic and topological standpoint. Acta Mater 183:93–109
85. Mohammed ASK, Sehitoglu H (2021) Strain-sensitive Topological Evolution of Twin Interfaces. Acta Materialia 208:116716
86. Kajiwara S, Kikuchi T (1982) Dislocation structures produced by reverse martensitic transformation in a Cu Zn alloy. Acta Metall 30(2):589–598

87. Kajiwara S, Kikuchi T (1983) Reversible movement of the austenite-martensite interface and dislocation structures in reverse-transformed austenite in Fe-Ni-C alloys. Philos Mag A 48(4):509–526
88. Sehitoglu H, Wu Y, Alkan S, Ertekin E (2017) Plastic deformation of B2-NiTi–is it slip or twinning? Philos Mag Lett 97(6):217–228
89. Tseng L, Ma J, Hornbuckle B, Karaman I, Thompson G, Luo Z, Chumlyakov Y (2015) The effect of precipitates on the superelastic response of [1 0 0] oriented FeMnAlNi single crystals under compression. Acta Mater 97:234–244
90. Tseng L, Ma J, Wang S, Karaman I, Kaya M, Luo Z, Chumlyakov Y (2015) Superelastic response of a single crystalline FeMnAlNi shape memory alloy under tension and compression. Acta Mater 89:374–383
91. Wu Y, Ertekin E, Sehitoglu H (2017) Elastocaloric cooling capacity of shape memory alloys–Role of deformation temperatures, mechanical cycling, stress hysteresis and inhomogeneity of transformation. Acta Mater 135:158–176
92. Bonnot E, Romero R, Mañosa L, Vives E, Planes A (2008) Elastocaloric effect associated with the martensitic transition in shape-memory alloys. Phys Rev Lett 100(12):125901
93. Ojha A, Sehitoglu H (2016) Transformation stress modeling in new FeMnAlNi shape memory alloy. Int J Plast 86:93–111
94. Liu Y, Xie Z, Van Humbeeck J, Delaey L (1998) Asymmetry of stress–strain curves under tension and compression for NiTi shape memory alloys. Acta Mater 46(12):4325–4338
95. Sidharth R, Abuzaid W, Vollmer M, Niendorf T, Sehitoglu H (2020) Fatigue crack initiation in the iron-based shape memory alloy FeMnAlNiTi. Shap Mem Superelasticity 6(3):323–331
96. Sehitoglu H, Karaman I, Anderson R, Zhang X, Gall K, Maier H, Chumlyakov Y (2000) Compressive response of NiTi single crystals. Acta Mater 48(13):3311–3326
97. Vollmer M, Bauer A, Kriegel MJ, Motylenko M, Niendorf T (2021) Functionally graded structures realized based on Fe–Mn–Al–Ni shape memory alloys. Scripta Materialia 194:113619